MATERIALS SCIENCE

Dislocation-driven growth of two-dimensional lateral quantum-well superlattices

Wu Zhou,[1,2*†] Yu-Yang Zhang,[1,3*] Jianyi Chen,[4] Dongdong Li,[1] Jiadong Zhou,[5] Zheng Liu,[5] Matthew F. Chisholm,[2] Sokrates T. Pantelides,[1,3] Kian Ping Loh[4]

The advent of two-dimensional (2D) materials has led to extensive studies of heterostructures for novel applications. 2D lateral multiheterojunctions and superlattices have been recently demonstrated, but the available growth methods can only produce features with widths in the micrometer or, at best, 100-nm scale and usually result in rough and defective interfaces with extensive chemical intermixing. Widths smaller than 5 nm, which are needed for quantum confinement effects and quantum-well applications, have not been achieved. We demonstrate the growth of sub–2-nm quantum-well arrays in semiconductor monolayers, driven by the climb of misfit dislocations in a lattice-mismatched sulfide/selenide heterointerface. Density functional theory calculations provide an atom-by-atom description of the growth mechanism. The calculated energy bands reveal type II alignment suitable for quantum wells, suggesting that the structure could, in principle, be turned into a "conduit" of conductive nanoribbons for interconnects in future 2D integrated circuits via n-type modulation doping. This misfit dislocation–driven growth can be applied to different combinations of 2D monolayers with lattice mismatch, paving the way to a wide range of 2D quantum-well superlattices with controllable band alignment and nanoscale width.

INTRODUCTION

Two-dimensional (2D) materials have attracted extensive research efforts in recent years due to their unique properties and promise in a wide range of applications (*1*–*4*). By stitching different 2D materials side by side or stacking them vertically layer by layer, heterostructures can be created with interesting optical and electronic properties emerging from the heterointerface due to the coupling between the different 2D components (*4*–*16*). In particular, the structural similarity among different semiconducting transition metal dichalcogenides has made it feasible to grow high-quality 2D lateral semiconductor heterostructures with atomically sharp interfaces via lateral epitaxy growth (*7*–*14*). Further combining lateral epitaxy growth with lithography patterning or multistep sequential growth, 2D multiheterojunctions or superlattices with featured width in the micrometer scale have also been demonstrated (*5*, *12*–*14*). However, these methods are limited in spatial resolution and usually produce rough or defective interfaces with extensive chemical intermixing (*5*, *12*–*14*). 2D lateral multiheterostructures or superlattices with width smaller than 5 nm, a regime where quantum size effect would come into play, have never been reported and remain a major challenge for 2D materials research.

Quantum-well structures in the 2D limit can, in principle, be created by laterally sandwiching a nanoscale strip of a 2D semiconductor between two strips of another 2D semiconductor with a different band gap. Because of their unique electronic structure and quantum confinement, quantum wells in conventional semiconductors have found important applications in quantum cascade lasers, infrared photodetectors, high–electron mobility transistors, high-efficiency thermoelectrics, and solar cells (*17*–*21*). In order for quantum size effects to take place, it is necessary to control the width of the 2D quantum well to be comparable to the de Broglie wavelength of the carriers (that is, in the sub–10-nm regime and ideally less than 5 nm).

Here, we report the growth of high-quality sub–2-nm-wide quantum wells within semiconductor monolayers, making use of the lattice mismatch between two semiconducting materials in the 2D lateral heterostructures. The growth is controlled by individual misfit dislocations formed at the lateral heterointerface between a selenide monolayer (WSe_2 or $MoSe_2$) and a sulfide monolayer (WS_2 or MoS_2). Atomic-resolution scanning transmission electron microscopy (STEM) images reveal that these sulfide quantum wells are less than 2 nm in width and form fully coherent lateral interfaces with the selenide monolayer matrix without extended defects. Density functional theory (DFT) calculations demonstrate that the strain field around the misfit dislocations makes them highly reactive during the heterostructure growth. We show that insertion of metal and S atoms into the dislocation cores induces dislocation climb, whereas concomitant selective substitution of Se atoms around the dislocation core by S atoms, driven by the local strain field, leads to growth of WS_2 and MoS_2 quantum-well arrays embedded in the WSe_2 and $MoSe_2$ monolayers. The regular dislocation spacing in the misfit array initially present at the lattice-mismatched interface results in nanoscale quantum-well arrays with periodic spacing. Because of the 2D nature of these structures, the quantum wells can also be thought of as ultranarrow nanoribbons. If doped to be metallic, these nanoribbons could serve as interconnects in future 2D integrated circuits (that is, the 2D material can serve as a "conduit" of conductive nanoribbons). Because misfit dislocations could form in periodic arrays at heterointerfaces, we expect that similar growth mechanisms can be used to fabricate 2D semiconductor quantum wells using different combinations of 2D monolayers with lattice mismatch and create a wide range of 2D quantum-well superlattices or nanoribbon conduits with controllable width and separation.

RESULTS

Figure 1A shows a WS_2 quantum well formed inside the WSe_2 monolayer in a lateral WSe_2/WS_2 heterostructure. Under our experimental

[1]School of Physical Sciences and CAS Center for Excellence in Topological Quantum Computation, University of Chinese Academy of Sciences, Beijing 100049, China. [2]Materials Science and Technology Division, Oak Ridge National Laboratory, Oak Ridge, TN 37831, USA. [3]Department of Physics and Astronomy and Department of Electrical Engineering and Computer Science, Vanderbilt University, Nashville, TN 37235, USA. [4]Department of Chemistry and Centre for Advanced 2D Materials, National University of Singapore, 3 Science Drive 3, Singapore 117546, Singapore. [5]School of Materials Science and Engineering, Nanyang Technological University, Singapore 639798, Singapore.
*These authors contributed equally to this work.
†Corresponding author. Email: wuzhou@ucas.ac.cn

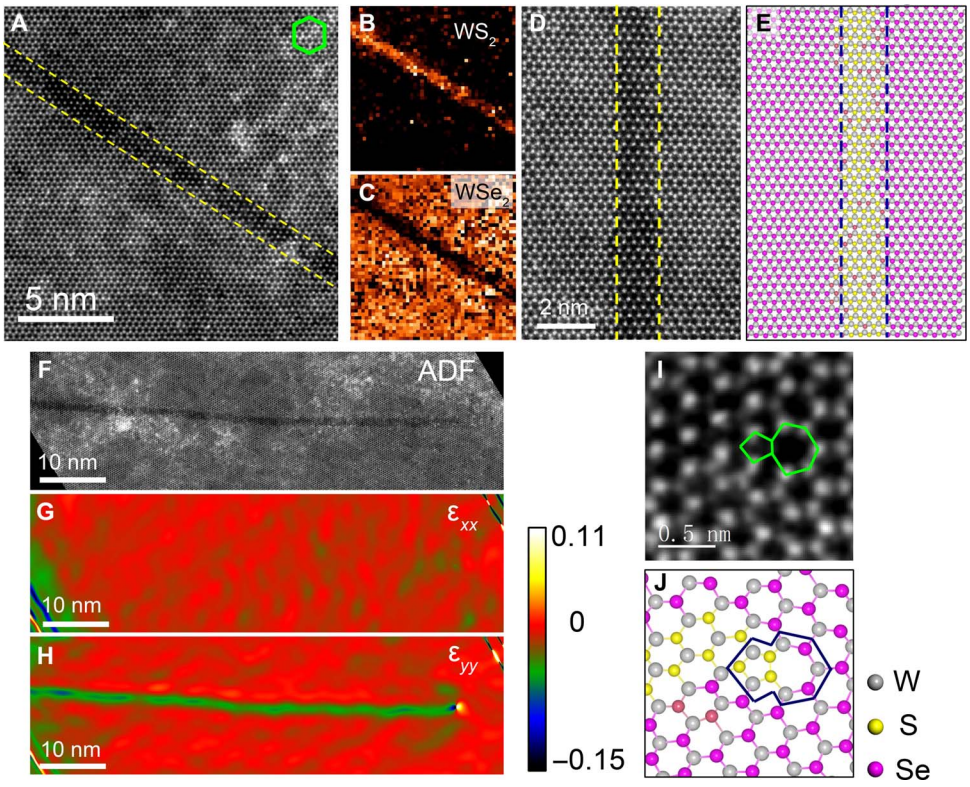

Fig. 1. Structure and strain analysis of a WS_2 quantum well embedded in a WSe_2 matrix. (**A**) Atomic-resolution STEM-ADF image of the embedded WS_2 quantum well with a width of 1.2 nm. The coherent interfaces between the WS_2 quantum well and the WSe_2 matrix are highlighted by the yellow dashed line. The hexagon highlights the orientation of the lattice. (**B** and **C**) Chemical mapping from the same region as in (A) showing the spatial distribution of WS_2 and WSe_2, respectively. (**D** and **E**) High-resolution STEM-ADF image of a WS_2 quantum well and the corresponding atomic structural model. The dashed lines highlight the coherent lateral interface along the armchair direction. (**F** to **H**) STEM-ADF of the entire 65-nm-long WS_2 quantum well and the corresponding strain distribution (see Materials and Methods) around the quantum well. (**I** and **J**) STEM-ADF image showing the atomic arrangement of the dislocation core at the tip of the WS_2 quantum well in (F) and the corresponding atomic model.

setup for STEM annular dark-field (ADF) imaging, the STEM-ADF image intensity for Se and S sites roughly follows $Z^{1.54}$, where Z is the atomic number, showing distinguishable atomic number contrast (*22*, *23*). As shown in Fig. 1A, the WS_2 monolayer strip displays lower image intensity than the surrounding WSe_2 matrix, where the lateral interfaces are highlighted by the yellow dashed lines. Chemical mapping using electron energy loss spectroscopy (EELS) imaging (see Materials and Methods and fig. S1), acquired simultaneously with the ADF image from the same region, further confirms that the darker strip is a WS_2 quantum well embedded within the WSe_2 monolayer, as shown in Fig. 1 (B and C). The bright background features in the ADF images are contaminates, mainly carbon and Si from the sample growth and TEM sample transfer, as confirmed by EELS mapping. Measuring from the atomic-resolution image, this WS_2 quantum well has a width of 1.2 nm (that is, four WS_2 unit cells in width).

Careful inspection of the ADF image reveals that the WS_2 quantum well grows along the armchair direction of the hexagonal lattice and forms fully coherent lateral interfaces with the WSe_2 matrix, free of any misfit dislocations or extended defects (Fig. 1, D and E). This is further confirmed by the strain analysis (see Fig. 1, F to H; fig. S2; and Materials and Methods) over the entire length of the WS_2 quantum well (65 nm in length, representing an aspect ratio over 50). Here, the perfect lattice from the WSe_2 monolayer is used as reference for calculating the strain. As shown in Fig. 1G, in parallel to the growth direction (x direction), the quantum well shows the same lattice spacing as the surrounding WSe_2 monolayer. The fact that the WSe_2 lattice constant is ~4% larger than WS_2 in perfect monolayers indicates a high and uniform tensile strain accommodated in the WS_2 quantum well along its growth direction, which leads to the observed dislocation-free lateral interface. In contrast, considerable difference (~4.3 ± 0.5%) in lattice spacing is observed between the WS_2 quantum well and the WSe_2 monolayer along the y direction (Fig. 1H), arising from the inherent lattice mismatch between the two materials. This lattice spacing difference is accommodated in a misfit dislocation core, composed of a pentagon-heptagon (5|7) pair (*24*–*26*), at the tip of the WS_2 quantum well, with the heptagon pointing away from the WS_2 (Fig. 1, I and J).

These ultranarrow WS_2 quantum wells are frequently observed in almost all the lateral WSe_2/WS_2 heterostructure samples (fig. S3) we have studied, growing in arrays from the heterointerface into the WSe_2 monolayer. As is well established in thin-film growth, strain relaxation at epitaxial heterointerfaces with inherent lattice mismatch can generate misfit dislocations once the film passes a certain critical thickness (*27*, *28*). For the lateral WSe_2/WS_2 heterostructure, because of the ~4% lattice mismatch, misfit dislocation arrays are expected to form at the lateral interface, with an average separation of ~8 nm along the zigzag direction (fig. S4), to relieve the lattice strain, as schematically shown in Fig. 2A (I). This is observed experimentally in the heterostructure samples. Figure 2 (B and C) shows such an epitaxial heterointerface with

quasi-periodic misfit dislocation arrays, where the heptagons at the dislocation cores all point into the WSe_2 lattice (fig. S5). However, in most of the samples, we observe these misfit dislocations propagating (or penetrating) into the 2D matrix, leaving a trace of arrays of the sub–2-nm-wide WS_2 quantum wells, as illustrated in Fig. 2A (II and III) and evidenced by Fig. 2 (D and E) and fig. S6. Statistical analysis reveals that these WS_2 quantum wells have an average width of 1.19 ± 0.09 nm (fig. S6C) (that is, four WS_2 unit cells in width). The fact that the WS_2 quantum wells are always growing from the lateral WSe_2/WS_2 heterointerface, with a single dislocation core at the growth front, indicates that the growth of the WS_2 quantum wells and climb of the misfit dislocations are intimately connected and that the growth is controlled by the dislocation.

To explore the atom-by-atom mechanism of the misfit dislocation–driven growth of quantum wells, we posited a scenario and then performed DFT calculations to validate it. A misfit dislocation, modeled as a 5|7 pair as shown in Fig. 3A, is created at the WSe_2/WS_2 interface for every 24 WSe_2 or 25 WS_2 unit cells to release lattice strain (fig. S4). Because the climb of the misfit dislocation from the interface into the WSe_2 lattice involves the insertion of an extra line of atoms, we consider the insertion of one W atom and two S atoms (highlighted by the blue circle in Fig. 3B, denoted as W-S_2 hereafter) from the gas

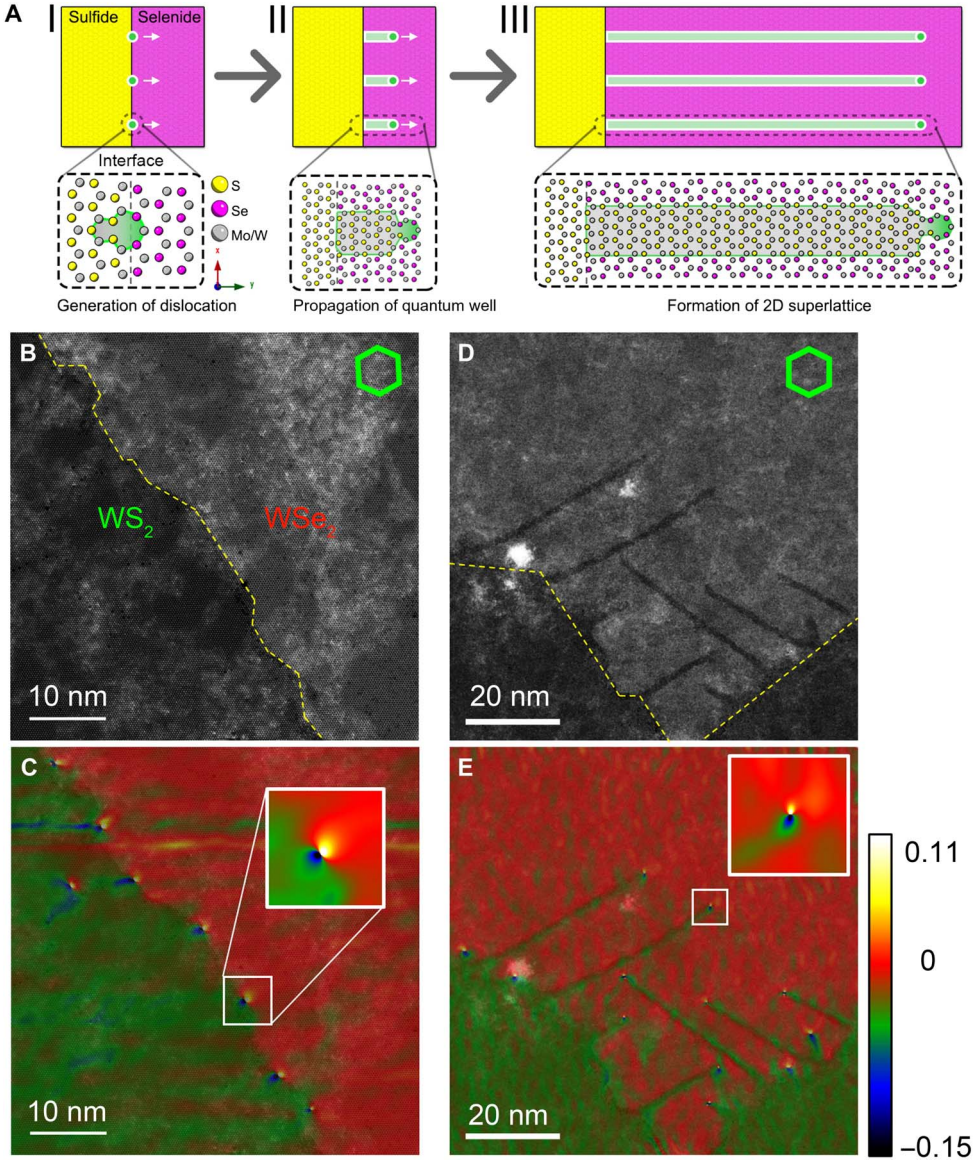

Fig. 2. Formation of periodic dislocation arrays and dislocation-driven growth of WS_2 quantum wells at the WSe_2/WS_2 lateral interface. (**A**) Schematic showing (I) the formation of periodic dislocation array, (II) dislocation-driven growth of WS_2 quantum wells, and (III) formation of 2D quantum-well superlattice in the WSe_2/WS_2 lateral heterostructure. (**B**) STEM-ADF image of a WSe_2/WS_2 lateral interface without the formation of WS_2 quantum wells. The epitaxial interface is highlighted by the yellow dashed line. (**C**) Corresponding strain distribution, overlaid onto the ADF image, showing the formation of periodic dislocation array at the heterointerface. (**D**) STEM-ADF image of a WSe_2/WS_2 lateral interface with the formation of WS_2 quantum wells. The WS_2 quantum wells appear as darker stripes with the same width. (**E**) Corresponding strain map, overlaid onto the ADF image, showing the presence of a dislocation core at the tip of each WS_2 quantum well. Insets in (C) and (E) are magnified views of the strain maps at the highlighted dislocation cores.

source into the 5|7 rings. This insertion pushes the 5|7 dislocation one unit cell forward into WSe_2 (that is, dislocation climb). If this step is followed by substitution of Se atoms by S atoms (denoted as S_{Se}) selectively in the pentagon and then right next to the 5|7 dislocation core (blue arrows in Fig. 3, B and C) to relieve local strain, a WS_2 nanoseed that is four unit cells wide and one unit cell long would penetrate into the WSe_2 monolayer (shaded in light blue in Fig. 3D). Repeating the above processes of W-S_2 insertion and subsequent three S_{Se} substitutions would lead to the growth of the WS_2 nanoseed into the WSe_2 lattice and ultimately form a WS_2 quantum well. An atomic model with six steps of dislocation climb and S_{Se} substitution is shown in Fig. 3G. It should be noted that based on this growth mechanism, the WS_2 quantum well should, on average, grow along the armchair direction, which is in excellent agreement with our experimental observations.

DFT calculations verified that the above scenario is energetically possible. We constructed a very large supercell accommodating 24 WSe_2 and 25 WS_2 unit cells (fig. S4), accommodating the lattice misfit by a 5|7 dislocation. For the insertion of a W-S_2 unit, we compared the competition between insertion into the dislocation core (that is, dislocation climb) and attachment to a straight or a stepped WS_2 edge (that is, growth at the fresh WS_2 edge) (fig. S7). The energy gain for edge growth is 2.45 eV at a step edge (fig. S7, C and D) and 3.53 eV at a straight edge (fig. S7, E and F), respectively. For comparison, insertion into a 5|7 dislocation core leads to an energy gain of 2.81 eV. These results suggest that the climb of misfit dislocations is energetically feasible and should occur in parallel with the heterostructure growth, given the availability of W and S atoms during the WS_2 growth.

We also evaluated the energetics of S_{Se} substitution. Using the DFT-based climbing image nudged elastic band (DFT-CINEB) method, we first calculated the substitution barrier in a perfect WSe_2 lattice (see Materials and Methods and fig. S8). As shown in Fig. 3E, the barrier for S_{Se} substitution in a perfect WSe_2 lattice is 3.8 eV, which indicates that S_{Se} substitution is unlikely to happen under the growth temperature of 700°C. This result is consistent with the experimental fact that we do not obtain alloying in the WSe_2 monolayer. However, this barrier can be significantly lowered by strain. We found that the S_{Se} substitution energy barrier drastically decreases to 2.6 eV (blue curve in Fig. 3E) under 4% compressive strain and lowers by 0.5 to 3.3 eV for 2% strain (see Materials and Methods). Bond length analysis in Fig. 3F, based on the DFT-relaxed interface structural model in Fig. 3B, shows that compressive strain is mainly distributed in and next to the pentagon of the 5|7 dislocation and quickly fades out as one goes further away from the dislocation core. Therefore, the calculations support the notion that the localized compressive strain at the misfit dislocation cores reduces the substitution energy barrier by a sufficient amount to make the S_{Se} substitution feasible and highly selective under typical growth conditions of the heterostructures (700°C).

Because the S_{Se} substitution process is governed by the strain field around the dislocation core at the growth front, we can expect that the WS_2 quantum wells have uniform width and a sharp coherent interface with the WSe_2 matrix over the entire length if a thermodynamically stable growth condition is maintained. Experimental results suggest that this is very promising. As demonstrated in Fig. 1 (E and D), this WS_2 quantum well shows a uniform width of 1.2 nm and an atomically sharp interface over a length of 12 nm. A small amount (~8%) of Se atoms remains inside the WS_2 quantum well due to incomplete S_{Se} substitution during the growth, which may well be eliminated if the growth conditions can be better controlled.

From the mechanism discussed above, we can expect these quantum wells to grow into equally spaced parallel arrays over macroscopic length scales (that is, forming a 2D quantum-well superlattice) starting with periodic misfit dislocations at the heterointerface, if mild growth conditions can be precisely controlled over a long period of time. The WS_2 quantum wells grown via this mechanism have a type II band alignment with the WSe_2 monolayer matrix as shown in Fig. 4A. Charge separation is a possible function of the WS_2/WSe_2 superlattice. In addition, the WS_2 quantum wells can also be thought of as ultranarrow nanoribbons. Because of the type II band alignment in the present system, if the material is doped n-type (for example, by Re atoms substituting W atoms in either WSe_2 or WS_2) (*29*), all the electrons would drop into the WS_2 pockets in the conduction bands, making the WS_2 nanoribbons conductive (fig. S9). This kind of "modulation doping" leads to high carrier mobilities because the ionized donors lie largely in the WSe_2 regions, which reduces the Coulomb scattering in the nanoribbons (*30*).

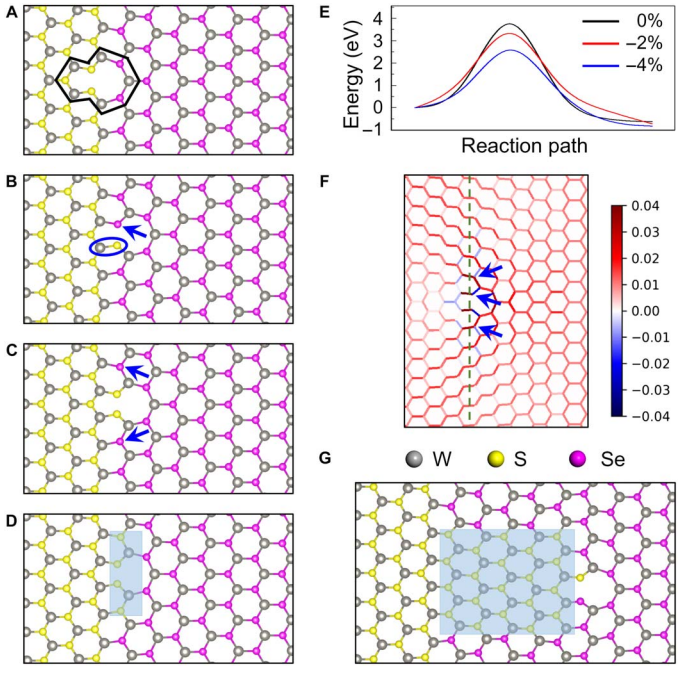

Fig. 3. Growth mechanism of the WS_2 quantum well in WSe_2. Atomic models of (**A**) 5|7 dislocation at the WS_2/WSe_2 interface due to lattice mismatch, (**B**) dislocation climbs one unit cell into WSe_2 by inserting a W atom and an S_2 pair, (**C**) substitution of Se by S in pentagon of the 5|7 dislocation, and (**D**) subsequent substitution of Se atoms next to the 5|7 dislocation by S resulting in a four–unit cell–wide WS_2 nanoseed. (**E**) Energy barrier for S_{Se} substitution under different levels of compressive strain. (**F**) Strain mapping based on bond length analysis for the atomic model in (B). See Materials and Methods for details. The green dashed line indicates the WS_2/WSe_2 interface. (**G**) Structural model showing a short WS_2 strip four unit cells wide and six unit cells long after repeating the insertion-substitution process six times.

DISCUSSION

On the basis of the results from the lateral WSe_2/WS_2 heterostructure system, we can expect that similar quantum-well superlattice structures can also form in lateral $MoSe_2/MoS_2$ heterostructures (fig. S10). Figure 4B shows such an example. Appearing as quasi-parallel narrow dark stripes across the whole image, these MoS_2 quantum wells are seen to extend more than a few hundred nanometers (although we were

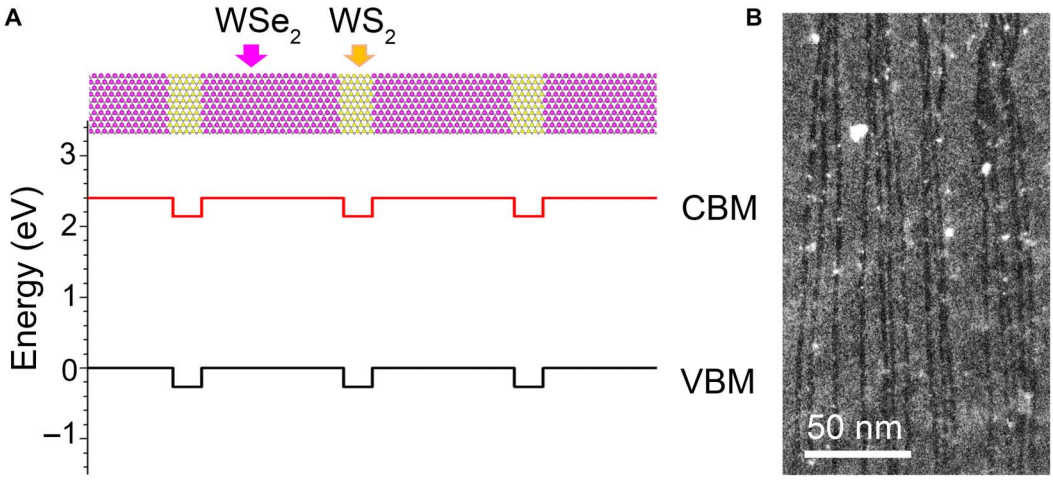

Fig. 4. Toward 2D quantum-well superlattice with atomically sharp lateral interfaces. (**A**) Atomic structural model and band alignment for a WSe_2/WS_2 superlattice calculated with the HSE06 functional. Valence band maximum (VBM) and conduction band minimum (CBM) are plotted by black and red lines, respectively. Yellow, S; purple, Se; gray, W. (**B**) Low-magnification STEM-ADF image showing the formation of parallel MoS_2 quantum wells of a few hundred nanometers long in a $MoSe_2$ monolayer toward the formation of quantum-well superlattice.

not able to see the entire length of these quantum wells due to the fracture and folding of the atomic film during TEM specimen transfer and the 1-μm visible window on the carbon support film) while still maintaining their general armchair growth direction and a uniform width of 1.8 ± 0.2 nm (that is, six unit cells). As can be noticed from the atomic mechanism illustrated in Fig. 3 (A and B), each dislocation climb step actually has a small component along the zigzag direction due to atomic reconstruction after the insertion of the W-S_2 units (fig. S11A). That is, the dislocation wiggles slightly sidewise around the armchair direction while climbing forward. Ideally, this small wiggling has equal probability toward both sides of the armchair direction (fig. S11A); therefore, the overall consequence is that the dislocation climbs and the corresponding quantum well grows along the armchair direction (movie S1). In the case when a few steps of dislocation climbing have the same sidewise component, a nanosized kink (see fig. S11B for an example) would develop, and as a consequence, the quantum wells would not look so straight and parallel at a larger scale. Nevertheless, each segment of the quantum wells still follows the general armchair growth direction.

Although the quantum wells shown in Fig. 4B are not evenly spaced, presumably because the misfit dislocations were not initially formed in a periodic array as those shown in Fig. 2C, we believe that this is an important demonstration toward the formation of 2D quantum-well superlattice at a length scale where quantum confinement would have a strong effect. With better control over the growth parameters of chemical vapor deposition (CVD) systems, or alternatively by using molecular beam epitaxy or metal-organic CVD techniques that are commonly used for the growth of bulk semiconductor superlattices, it is very promising that high-quality 2D semiconductor quantum-well superlattices can be grown via this dislocation-driven mechanism.

The successful growth of quantum-well arrays in both WSe_2/WS_2 and $MoSe_2/MoS_2$ lateral heterostructures suggests that this misfit dislocation–driven growth mechanism should apply in a much broader combination of 2D monolayers with lattice mismatch given their structural similarities. For example, $NbSe_2$ and $MoSe_2$ monolayers share the same 2H structure but with ~4.5% lattice mismatch (a = 3.44 Å for $NbSe_2$ and 3.29 Å for $MoSe_2$), which should lead to misfit dislocation arrays with average spacing of 7.5 nm at the lateral heterointerface and, consequently, quantum-well superlattices with average separation of 7.5 nm. Considering the wide spectrum of electronic and optical properties in various 2D monolayers, including topological insulators and superconductors, this opens exciting opportunities to create a large family of 2D quantum wells and their superlattices with novel properties.

MATERIALS AND METHODS

Growth of the WSe_2/WS_2 heterostructures

The WSe_2/WS_2 heterojunctions were grown on SiO_2/Si substrates using a two-step ambient pressure CVD method (*12*). WO_3 powder (about 5.0 mg) was placed on SiO_2/Si growth substrates and located in the heating zone center of the furnace. Se powder (1.2 g) was placed in a quartz test tube at the upper stream side as the source for the selenization of WO_3. H_2 [2.2 standard cubic centimeter per minute (sccm)] and Ar (20 sccm) were used as the carrier gas. The center heating zone was heated to 700°C at a ramping rate of 20°C/min. As the temperature approached 700°C, the temperature of the Se powder was maintained at ~280°C. After a 30-min growth at 700°C, the furnace was naturally cooled down to room temperature in a gas flow of 5 sccm H_2 and 20 sccm Ar. The growth substrate with WSe_2 crystals and WO_3 powder (as W precursor) on the surface was transferred to another CVD system for WS_2 growth. Similarly, a smaller quartz test tube containing 0.8 g of sulfur powder was located upstream as S precursor. Notably, the growth substrate was kept out of the furnace during the heating stage. As the temperature approached 700°C, the heating zone in the furnace was adjusted by moving the furnace to set the temperature of the S powders at ~180°C and the temperature of the substrates at ~700°C. After a 15-min growth at 700°C, the furnace was cooled down to room temperature quickly.

Growth of the $MoSe_2/MoS_2$ heterostructures

A two-step CVD method was used for the growth of the $MoSe_2/MoS_2$ lateral heterostructures. Briefly, the $MoSe_2$ monolayer was first grown by a CVD method in a 5.08-cm tube. A mixed Ar/H_2 flow of 80:5 sccm was used as the carrier gas, and a silicon boat containing 10 mg of MoO_3 was put in the center of the tube. The SiO_2/Si substrate was placed on the boat with surface downside. Another silicon boat containing 0.5 g of Se powder was located on the upstream. The temperature ramped up

to 750°C in 15 min, where it was kept for about 10 min. The as-grown $MoSe_2$ was then transferred into another CVD setup for subsequent MoS_2 growth. For the growth of MoS_2, Ar flow of 60 sccm was used as the carrier gas, and a silicon boat containing 10 mg of MoO_3 was put in the center of a 2.54-cm tube. The $MoSe_2/SiO_2/Si$ substrate was placed on the boat with surface downside. Another silicon boat containing 0.5 g of S powder was located on the upstream. The temperature was ramped up to 650°C in 13 min and was kept there for about 5 min.

Electron microscopy experiments

The TEM samples were prepared with a poly(methyl methacrylate) (PMMA)–assisted method. A layer of PMMA about 1 μm thick was spin-coated on the wafer with heterostructure samples deposited and then baked at 180°C for 3 min. Afterward, the wafer was immersed in NaOH solution (1 M) to etch the SiO_2 layer overnight. After liftoff, the sample was transferred into deionized water for several cycles to wash away the residual contaminants, and then it was fished by a TEM grid. For the WSe_2/WS_2 lateral heterostructure samples, conventional lacey carbon film TEM grids, with random holes of 1 to 5 μm in diameter, were used. Quantifoil grids with regular 1-μm holes were used for the $MoSe_2/MoS_2$ lateral heterostructure samples. The as-transferred specimen was dried naturally in ambient environment and then dropped into acetone overnight to wash away the PMMA coating layers.

To avoid hydrocarbon contamination, all the TEM samples were baked at 160°C for 8 hours under vacuum before the microscopy experiment. STEM imaging and EELS analysis were performed on a Nion UltraSTEM 100 equipped with a cold field-emission gun and a fifth-order aberration corrector operating at 60 kV. The convergence semi-angle for the incident probe was 31 mrad. The ADF images were collected for a half-angle range of ~86 to 200 mrad. The collection semi-angle for EELS was set to 48 mrad. The WSe_2 and WS_2 maps were obtained by multiple linear least-squares fitting of the experimental EELS spectrum image with the reference spectra from pure WSe_2 and WS_2 monolayers (fig. S1), acquired under the same experimental conditions. Strain analysis was performed on the basis of the geometric phase analysis method (*31*) using the FRWRtools plugin (www.physics.hu-berlin.de/en/sem/software/software_frwrtools) for DigitalMicrograph. The strain was calculated using the perfect WSe_2 lattice as reference. All STEM experiments were performed at room temperature.

Theoretical calculations

Quantum mechanical calculations based on DFT were performed using the Vienna Ab initio Simulation Package (VASP) (*32*, *33*). The projector augmented wave method was used to describe the core electrons (*34*). The Perdew-Becke-Ernzerhof (PBE) functional was used for exchange and correlation (*35*). The theoretical calculated lattice constants of WSe_2 and WS_2 were 3.315 and 3.181 Å, respectively, which are in agreement with experimental values (3.282 Å for WSe_2 and 3.153 Å for WS_2) (*36*). The atomic model we used is shown in fig. S3. In the *y* direction, we used 24 units of WSe_2 (79.56 Å), which matched 25 units of WS_2 (79.53 Å). In the *x* direction, the supercell contained four WS_2 hexagons, six WSe_2 hexagons, and a vacuum layer larger than 15 Å. In the *z* direction, a vacuum layer larger than 15 Å was used. Because of the large size of the supercell, a 259-eV energy cutoff and Γ-only *k*-point sampling were used for structure relaxation and energy band calculations. Total energies were converged to 10^{-4} eV, and forces were converged to 0.02 eV/Å.

Energy barriers for the S_{Se} substitution were calculated using the CI-NEB method (*37*, *38*). A (5 × 5) WSe_2 supercell was used to model the WSe_2 basal plane. A 3 × 3 Γ-center *k*-grid mesh was used to sample the first Brillouin zone (*39*). Four images were inserted between initial and final states. Calculation of the substitution energy barrier in the big supercell containing a heterostructure with a dislocation (fig. S3) was not practical. Instead, we applied different levels of compressive strain to the otherwise perfect WSe_2 monolayer to model the effect of compressive strain on the energy barrier for the S_{Se} substitution.

The strain mapping shown in Fig. 3E in the main text was obtained by comparing the bond length in the DFT-optimized atomic model of the 5|7 dislocation at the WS_2/WSe_2 interface (Fig. 3B) to the standard bond lengths in pristine WS_2 and WSe_2 (that is, 2.39 Å for W-S bonds and 2.52 Å for W-Se bonds) (*40*). Specifically, we used the following formulae to calculate the bond strain, ε_{W-S} for W-S bonds and ε_{W-Se} for W-Se bonds

$$\varepsilon_{W\text{-}S} = \frac{d_{W\text{-}S} - 2.39}{2.39}$$
$$\varepsilon_{W\text{-}Se} = \frac{d_{W\text{-}Se} - 2.52}{2.52}$$

where $d_{W\text{-}S}$ and $d_{W\text{-}Se}$ are measured bond lengths for the W-S and W-Se bonds, respectively, in the structural model.

The energy band alignment of a lateral WSe_2/WS_2 superlattice was examined by calculations at different theoretical levels. A 20 WSe_2/5 WS_2 superlattice was set up. Atomic structures were fully relaxed at the PBE level with a fixed 79.56 Å lattice constant in the *y* direction (24 WSe_2 units) and 3.38 Å lattice constant in the *x* direction (1 WSe_2 unit). Energy band alignment was calculated at both PBE and HSE06 levels, in which a portion α = 25% of exact nonlocal Hartree-Fock exchange was mixed (*41*). Both calculations showed a type II band alignment.

SUPPLEMENTARY MATERIALS

Supplementary material for this article is available at http://advances.sciencemag.org/cgi/content/full/4/3/eaap9096/DC1

fig. S1. Reference EELS spectra from pure WSe_2 and WS_2 monolayers.
fig. S2. STEM-ADF of the entire 65-nm-long WS_2 quantum well and the corresponding strain distribution around the quantum well.
fig. S3. Optical images and spectroscopy measurements of the WSe_2/WS_2 lateral heterostructure.
fig. S4. Atomic model of WSe_2/WS_2 heterostructure.
fig. S5. Additional structural characterization data from the lateral WSe_2/WS_2 heterointerface.
fig. S6. Additional low-magnification STEM-ADF images showing the formation of arrays of WS_2 quantum wells at the WSe_2/WS_2 lateral interface, driven by dislocations.
fig. S7. Comparison between dislocation climb and extension of a WS_2 edge during the sample growth.
fig. S8. Atomic models for the S_{Se} substitution barrier calculations.
fig. S9. Band structure of lateral WSe_2/WS_2 superlattice.
fig. S10. Optical images and spectroscopy measurements of the $MoSe_2/MoS_2$ lateral heterostructure.
fig. S11. Dislocation climb and formation of nanosize kinks during the growth of quantum well.
movie S1. Scheme showing the dislocation climb and the corresponding quantum well growth process.

REFERENCES AND NOTES

1. K. S. Novoselov, A. K. Geim, S. V. Morozov, D. Jiang, Y. Zhang, S. V. Dubonos, I. V. Grigorieva, A. A. Firsov, Electric field effect in atomically thin carbon films. *Science* **306**, 666–669 (2004).
2. K. S. Novoselov, V. I. Fal'ko, L. Colombo, P. R. Gellert, M. G. Schwab, K. Kim, A roadmap for graphene. *Nature* **490**, 192–200 (2012).
3. G. R. Bhimanapati, Z. Lin, V. Meunier, Y. Jung, J. Cha, S. Das, D. Xiao, Y. Son, M. S. Strano, V. R. Cooper, L. Liang, S. G. Louie, E. Ringe, W. Zhou, S. S. Kim, R. R. Naik, B. G. Sumpter, H. Terrones, F. Xia, Y. Wang, J. Zhu, D. Akinwande, N. Alem, J. A. Schuller, R. E. Schaak, M. Terrones, J. A. Robinson, Recent advances in two-dimensional materials beyond graphene. *ACS Nano* **9**, 11509–11539 (2015).

4. A. K. Geim, I. V. Grigorieva, Van der Waals heterostructures. *Nature* **499**, 419–425 (2013).
5. Z. Liu, L. Ma, G. Shi, W. Zhou, Y. Gong, S. Lei, X. Yang, J. Zhang, J. Yu, K. P. Hackenberg, A. Babakhani, J.-C. Idrobo, R. Vajtai, J. Lou, P. M. Ajayan, In-plane heterostructures of graphene and hexagonal boron nitride with controlled domain sizes. *Nat. Nanotechnol.* **8**, 119–124 (2013).
6. L. Liu, J. Park, D. A. Siegel, K. F. McCarty, K. W. Clark, W. Deng, L. Basile, J. C. Idrobo, A.-P. Li, G. Gu, Heteroepitaxial growth of two-dimensional hexagonal boron nitride templated by graphene edges. *Science* **343**, 163–167 (2014).
7. X. Duan, C. Wang, J. C. Shaw, R. Cheng, Y. Chen, H. Li, X. Wu, Y. Tang, Q. Zhang, A. Pan, J. Jiang, R. Yu, Y. Huang, X. Duan, Lateral epitaxial growth of two-dimensional layered semiconductor heterojunctions. *Nat. Nanotechnol.* **9**, 1024–1030 (2014).
8. Y. Gong, J. Lin, X. Wang, G. Shi, S. Lei, Z. Lin, X. Zou, G. Ye, R. Vajtai, B. I. Yakobson, H. Terrones, M. Terrones, B. K. Tay, J. Lou, S. T. Pantelides, Z. Liu, W. Zhou, P. M. Ajayan, Vertical and in-plane heterostructures from WS_2/MoS_2 monolayers. *Nat. Mater.* **13**, 1135–1142 (2014).
9. C. Huang, S. Wu, A. M. Sanchez, J. J. P. Peters, R. Beanland, J. S. Ross, P. Rivera, W. Yao, D. H. Cobden, X. Xu, Lateral heterojunctions within monolayer $MoSe_2$–WSe_2 semiconductors. *Nat. Mater.* **13**, 1096–1101 (2014).
10. Y. Gong, S. Lei, G. Ye, B. Li, Y. He, K. Keyshar, X. Zhang, Q. Wang, J. Lou, Z. Liu, R. Vajtai, W. Zhou, P. M. Ajayan, Two-step growth of two-dimensional WSe_2/$MoSe_2$ heterostructures. *Nano Lett.* **15**, 6135–6141 (2015).
11. M.-Y. Li, Y. Shi, C.-C. Cheng, L.-S. Lu, Y.-C. Lin, H.-L. Tang, M.-L. Tsai, C.-W. Chu, K.-H. Wei, J.-H. He, W.-H. Chang, K. Suenaga, L.-J. Li, Epitaxial growth of a monolayer WSe_2-MoS_2 lateral p-n junction with an atomically sharp interface. *Science* **349**, 524–528 (2015).
12. J. Chen, W. Zhou, W. Tang, B. Tian, X. Zhao, H. Xu, Y. Liu, D. Geng, S. J. R. Tan, W. Fu, K. P. Loh, Lateral epitaxy of atomically sharp WSe_2/WS_2 heterojunctions on silicon dioxide substrates. *Chem. Mater.* **28**, 7194–7197 (2016).
13. M. Mahjouri-Samani, M.-W. Lin, K. Wang, A. R. Lupini, J. Lee, L. Basile, A. Boulesbaa, C. M. Rouleau, A. A. Puretzky, I. N. Ivanov, K. Xiao, M. Yoon, D. B. Geohegan, Patterned arrays of lateral heterojunctions within monolayer two-dimensional semiconductors. *Nat. Commun.* **6**, 7749 (2015).
14. Z. Zhang, P. Chen, X. Duan, K. Zang, J. Luo, X. Duan, Robust epitaxial growth of two-dimensional heterostructures, multiheterostructures, and superlattices. *Science* **357**, 788–792 (2017).
15. X. Ling, Y. Lin, Q. Ma, Z. Wang, Y. Song, L. Yu, S. Huang, W. Fang, X. Zhang, A. L. Hsu, Y. Bie, Y.-H. Lee, Y. Zhu, L. Wu, J. Li, P. Jarillo-Herrero, M. Dresselhaus, T. Palacios, J. Kong, Parallel stitching of 2D materials. *Adv. Mater.* **28**, 2322–2329 (2016).
16. L. Chen, L. He, H. S. Wang, H. Wang, S. Tang, C. Cong, H. Xie, L. Li, H. Xia, T. Li, T. Wu, D. Zhang, L. Deng, T. Yu, X. Xie, M. Jiang, Oriented graphene nanoribbons embedded in hexagonal boron nitride trenches. *Nat. Commun.* **8**, 14703 (2017).
17. L. Esaki, R. Tsu, Superlattice and negative differential conductivity in semiconductors. *IBM J. Res. Dev.* **14**, 61–65 (1970).
18. R. Tsu, L. Esaki, Tunneling in a finite superlattice. *Appl. Phys. Lett.* **22**, 562–564 (1973).
19. L. D. Hicks, T. C. Harman, M. S. Dresselhaus, Use of quantum-well superlattice to obtain a high figure of merit from nonconvential thermoelectric materials. *Appl. Phys. Lett.* **63**, 3230–3232 (1993).
20. J. Faist, F. Capasso, D. L. Sivco, C. Sirtori, A. L. Hutchinson, A. Y. Cho, Quantum cascade laser. *Science* **264**, 553–556 (1994).
21. M. S. Gudiksen, L. J. Lauhon, J. Wang, D. C. Smith, C. M. Lieber, Growth of nanowire superlattice structures for nanoscale photonics and electronics. *Nature* **415**, 617–620 (2002).
22. O. L. Krivanek, M. F. Chisholm, V. Nicolosi, T. J. Pennycook, G. J. Corbin, N. Dellby, M. F. Murfitt, C. S. Own, Z. S. Szilagyi, M. P. Oxley, S. T. Pantelides, S. J. Pennycook, Atom-by-atom structural and chemical analysis by annular dark-field electron microscopy. *Nature* **464**, 571–574 (2010).
23. W. Zhou, M. P. Oxley, A. R. Lupini, O. L. Krivanek, S. J. Pennycook, J.-C. Idrobo, Single atom microscopy. *Microsc. Microanal.* **18**, 1342–1354 (2012).
24. X. Zou, Y. Liu, B. I. Yakobson, Predicting dislocations and grain boundaries in two-dimensional metal-disulfides from the first principles. *Nano Lett.* **13**, 253–258 (2013).
25. W. Zhou, X. Zou, S. Najmaei, Z. Liu, Y. Shi, J. Kong, J. Lou, P. M. Ajayan, B. I. Yakobson, J.-C. Idrobo, Intrinsic structural defects in monolayer molybdenum disulfide. *Nano Lett.* **13**, 2615–2622 (2013).
26. S. Najmaei, Z. Liu, W. Zhou, X. Zou, G. Shi, S. Lei, B. I. Yakobson, J.-C. Idrobo, P. M. Ajayan, J. Lou, Vapour phase growth and grain boundary structure of molybdenum disulphide atomic layers. *Nat. Mater.* **12**, 754–759 (2013).
27. J. W. Matthews, A. E. Blakeslee, Defects in epitaxial multilayers. 1. Misfit dislocations. *J. Cryst. Growth* **27**, 118–125 (1974).
28. S. C. Jain, A. H. Harker, R. A. Cowley, Misfit strain and misfit dislocations in lattice mismatched epitaxial layers and other systems. *Philos. Mag. A* **75**, 1461–1515 (1997).
29. Y.-C. Lin, D. O. Dumcenco, H.-P. Komsa, Y. Niimi, A. V. Krasheninnikov, Y.-S. Huang, K. Suenaga, Properties of individual dopant atoms in single-layer MoS_2: Atomic structure, migration, and enhanced reactivity. *Adv. Mater.* **26**, 2857–2861 (2014).
30. J. L. Boland, S. Conesa-Boj, P. Parkinson, G. Tütüncüoglu, F. Matteini, D. Rüffer, A. Casadei, F. Amaduzzi, F. Jabeen, C. L. Davies, H. J. Joyce, L. M. Herz, A. Fontcuberta i Morral, M. B. Johnston, Modulation doping of GaAs/AlGaAs core-shell nanowires with effective defect passivation and high electron mobility. *Nano Lett.* **15**, 1336–1342 (2015).
31. M. J. Hytch, E. Snoeck, R. Kilaas, Quantitative measurement of displacement and strain fields from HREM micrographs. *Ultramicroscopy* **74**, 131–146 (1998).
32. G. Kresse, J. Furthmüller, Efficient iterative schemes for ab initio total-energy calculations using a plane-wave basis set. *Phys. Rev. B* **54**, 11169–11186 (1996).
33. G. Kresse, J. Furthmuller, Efficiency of ab-initio total energy calculations for metals and semiconductors using a plane-wave basis set. *Comput. Mater. Sci.* **6**, 15–50 (1996).
34. P. E. Blöchl, Projector augmented-wave method. *Phys. Rev. B* **50**, 17953–17979 (1994).
35. J. P. Perdew, K. Burke, M. Ernzerhof, Generalized gradient approximation made simple. *Phys. Rev. Lett.* **77**, 3865–3868 (1996).
36. J. Kang, S. Tongay, J. Zhou, J. Li, J. Wu, Band offsets and heterostructures of two-dimensional semiconductors. *Appl. Phys. Lett.* **102**, 012111 (2013).
37. G. Henkelman, B. P. Uberuaga, H. Jónsson, A climbing image nudged elastic band method for finding saddle points and minimum energy paths. *J. Chem. Phys.* **113**, 9901–9904 (2000).
38. G. Henkelman, H. Jónsson, Improved tangent estimate in the nudged elastic band method for finding minimum energy paths and saddle points. *J. Chem. Phys.* **113**, 9978–9985 (2000).
39. M. Methfessel, A. T. Paxton, High-precision sampling for Brillouin-zone integration in metals. *Phys. Rev. B* **40**, 3616–3621 (1989).
40. T. P. Kaloni, L. Kou, T. Frauenheim, U. Schwingenschlögl, Quantum spin Hall states in graphene interacting with WS_2 or WSe_2. *Appl. Phys. Lett.* **105**, 233112 (2014).
41. J. Heyd, G. E. Scuseria, M. Ernzerhof, Hybrid functionals based on a screened coulomb potential. *J. Chem. Phys.* **118**, 8207–8215 (2003).

Acknowledgments: Dedicated to the 80th birthday of Prof. Jing Zhu. We thank X. Zhao for help with the x-ray photoelectron spectroscopy measurement. **Funding:** This research was supported by the National Natural Science Foundation of China (51622211); the Key Research Program of the Chinese Academy of Sciences (CAS) (XDPB08-1); the CAS Pioneer Hundred Talents Program; the CAS Key Research Program of Frontier Sciences; the U.S. Department of Energy, Office of Science, Basic Energy Sciences, Materials Science and Engineering Division; and through a user project supported by Oak Ridge National Laboratory's Center for Nanophase Materials Sciences, which is sponsored by the Scientific User Facilities Division of U.S. Department of Energy (DOE). A portion of the research was performed at the CAS Key Laboratory of Vacuum Physics. Work at Vanderbilt was supported by the DOE (grant DE-FG02-09ER46554) and by the McMinn Endowment. This research is also supported by the Singapore National Research Foundation under NRF RF award no. NRF-RF2013-08, Tier 2 MOE2016-T2-2-153, and MOE2015-T2-2-007. Computations were carried out at the National Energy Research Scientific Computing Center, a DOE Office of Science User Facility supported by the Office of Science of the DOE under contract no. DE-AC02-05CH11231. **Author contributions:** W.Z. conceived the idea, performed the electron microscopy experiments, and wrote the paper. D.L. and M.F.C. participated in the electron microscopy data analysis. Y.-Y.Z. and S.T.P. performed the theoretical calculations. J.C. and K.P.L. provided the WSe_2/WS_2 heterostructure sample. J.Z. and Z.L. provided the $MoSe_2$/MoS_2 heterostructure sample. All authors discussed the results and commented on the manuscript. **Competing interests:** The authors declare that they have no competing interests. **Data and materials availability:** All data needed to evaluate the conclusions in the paper are present in the paper and/or the Supplementary Materials. Additional data related to this paper may be requested from the authors.

Submitted 12 September 2017
Accepted 10 February 2018
Published 23 March 2018
10.1126/sciadv.aap9096

Citation: W. Zhou, Y.-Y. Zhang, J. Chen, D. Li, J. Zhou, Z. Liu, M. F. Chisholm, S. T. Pantelides, K. P. Loh, Dislocation-driven growth of two-dimensional lateral quantum-well superlattices. *Sci. Adv.* **4**, eaap9096 (2018).

Dislocation-driven growth of two-dimensional lateral quantum-well superlattices

Wu Zhou, Yu-Yang Zhang, Jianyi Chen, Dongdong Li, Jiadong Zhou, Zheng Liu, Matthew F. Chisholm, Sokrates T. Pantelides and Kian Ping Loh

Sci Adv **4** (3), eaap9096.
DOI: 10.1126/sciadv.aap9096